Eur. Phys. J. Plus (2024) 139:967
https://doi.org/10.1140/epjp/s13360-024-05763-2

THE EUROPEAN PHYSICAL JOURNAL PLUS

Regular Article

Optical properties of a hollow cylindrical quantum wire in a parallel applied magnetic field

Moletlanyi Tshipa[1,a], **Monkami Masale**[1,b], **Kawtar Feddi**[2,c], **Laura M. Pérez**[3,d], **Elmustapha Feddi**[4,5,e]

[1] Department of Physics, University of Botswana, Corner of Mabuto and Notwane, Gaborone, Botswana
[2] Renewable Energy and Advanced Materials Laboratory, International University of Rabat, 10100 Rabat, Morocco
[3] Departamento de Ingeniería Industrial y de Sistemas, Universidad de Tarapacá, Casilla 7D, Arica 1000000, Chile
[4] Institute of Applied Physics, Mohammed VI Polytechnic University, Hay Moulay Rachid, Ben Guerir, 43150 Ben Guerir, Morocco
[5] Group of Optoelectronic of Semiconductors and Nanomaterials, Mohammed V University in Rabat, 10100 Rabat, Morocco

Received: 11 July 2024 / Accepted: 20 October 2024
© The Author(s) 2024

Abstract In this theoretical study, we investigate optical properties of a hollow cylindrical quantum wire in the presence of a homogeneous magnetic field. The magnetic field is applied parallel to the axis of the quantum wire. The investigations were achieved by solving the Schrödinger equation within the effective mass approximation. The optical properties studied were absorption coefficient (AC) of electromagnetic radiation and changes in refractive index (CRI) of the hollow cylinder. The parallel applied magnetic field lifts the degeneracy of states of opposite angular momentum (the $\pm|m|$ states, m being the angular momentum quantum number) known as the Zeeman splitting. As such, in the presence of magnetic field, AC splits into two branches, one corresponding to a transition involving the positive m states and the other corresponding to a transition involving the negative m states. Increase in intensity of the electromagnetic radiation reduces the magnitude of the AC. Presence of inner radius of the hollow cylindrical wire lowers transition energies. Apart from absorption due to the ($m = 0 \rightarrow \pm 1$) transitions, the presence of the inner radius also facilitates absorption due the ($m = -1 \rightarrow 0$) transition as the magnetic field strength increases, a phenomenon that does not happen in solid cylindrical quantum wires. The presence of the inner radius also enhances AC in strong magnetic field. Increase in intensity of the electromagnetic radiation affects the CRI (here considered up to third order), introducing a normal dispersion region in an otherwise anomalous region. The parallel magnetic field also splits the CRI depending on the sign of the m states involved in the transitions.

1 Introduction

Over the last decades, there has been a significant surge of interest surrounding nanostructures. This wide interest is explained by their exceptionally small dimensions, exhibiting distinct behaviors compared to bulk materials, primarily due to the effects of quantum confinement [1]. The quantization effects in semiconductors can be classified based on whether the charge carriers are confined in one, two, or three dimensions [2]. The increasing interest in investigating nanostructures can be traced back to the pioneering experimental work of Wagner and Eliss [3], who utilized the molecular beam epitaxy (MBE) technique to cultivate single silicon whiskers with minute diameters.

Since that pivotal work, semiconductor nanowires, characterized by their slender profiles, have inspired many researchers. This special geometry has spurred theoretical explorations, such as Zeng et al.'s investigation into the optical properties of ZnS/CdSe cylindrical quantum dot quantum wells (QDQW) [4] and AlGaAs/GaAs semi-parabolic quantum wells [5]. Furthermore, Nammas et al. have conducted two comprehensive theoretical studies [6, 7] on the thermodynamic properties of two and a few electrons in quantum dots (QDs), employing a harmonic potential to describe confinement. These studies have illuminated intriguing behaviors, revealing that mean energy exhibits a gradual rise at low temperatures, transitioning to a more rapid increase at higher temperatures. This contrasting behavior compared to heat capacity, which exhibits rapid growth at low temperatures followed by saturation as

Monkami Masale, Kawtar Feddi, Laura M. Pérez and Elmustapha Feddi have contributed equally to this work.

[a] e-mail: tshipam@ub.ac.bw (corresponding author)
[b] e-mail: masalem@ub.ac.bw
[c] e-mail: kawtar.feddi@uir.ac.ma
[d] e-mail: lperez@academicos.uta.cl
[e] e-mail: e.feddi@um5r.ac.ma

Published online: 04 November 2024

temperatures rise, mirrors observations in bulk materials. Jahan et al. [8] have also explored the impact of confinement potential shape on electronic, thermodynamic, magnetic, and transport properties in GaAs quantum dots. They noted a paramagnetic–diamagnetic transition influenced by the magnetic field.

The quest for understanding confinement effects continues with studies by Nguyen and Peeters [9], who investigated electron—electron correlations in multi-electron QDs under parabolic potential confinement. Their work delved into the energy spectrum, addition energy, and thermodynamic properties, revealing intriguing cusps in energy levels in their variation with applied magnetic field that manifest as peaks in heat capacity and susceptibility. Similar investigations extend to GaAs QDs with Gaussian confinement, as studied by B. Boyaciogly and Chatterjee [10], further emphasizing the importance of confinement nature. Moreover, Gumber et al.'s research [11, 12] into thermal and magnetic properties of quantum dots under parabolic confinement uncovered constant specific heat regions influenced by magnetic fields and temperatures. They also demonstrated the impact of the Rashba effect on the thermodynamic behavior of InSb QDs under magnetic fields. Recently, Yong Son et. al. have developed an interesting theoretical investigation concerning the infrared absorption of polaron with spin-orbit coupling in monolayer transition metal dichalcogenides, in which the polaron states are formed arising from the electron coupled with the intrinsic longitudinal optical phonon and the induced surface optical phonon modes [13]. The same authors have shown the existence of magnetopolaron resonance states in graphene in the strong magnetic field based on the Huybrechts's model, in which polaron states are formed due to the strong coupling between electrons and surface optical (SO) phonons induced by the polar substrate [14].

Moving beyond traditional nanostructures, core-shell quantum dots (CSQDs) have gained prominence due to their chemical stability and tunable dimensions. CSQDs find applications in diverse optoelectronic devices, including solar cells, lasers, and quantum light-emitting diodes [15–19]. Precisely controlling core and shell dimensions in CSQDs has become imperative, as their optical and electronic properties are intricately linked to these parameters [20–23]. In a comprehensive review article, Kyoung-Ho Kim and You-Shin No [24] introduced innovative plasmonic and metamaterial devices based on one-dimensional subwavelength nanostructures with cylindrical symmetry. Their work offers insights into optimizing core-shell quantum dots and selecting suitable materials for efficient electromagnetic wave manipulation.

Furthermore, the realm of nanostructures extends to hollow cylindrical nanostructures, including quantum rings (QRs) and hollow cylinders (HCs). Barseghyan et al. [25] conducted a numerical study assessing the influence of hydrostatic pressure, impurity position, and electric and magnetic fields on the binding energy and photo-ionization cross section of hydrogenic donor impurities within InAs Pöschl–Teller quantum rings. Their findings underscore the impact of external fields and confinement potential asymmetry on binding energy, with hydrostatic pressure playing a pivotal role. Additionally, Khordad and Sedehi [26] conducted an extensive investigation of the thermodynamic properties of a GaAs double ring-shaped quantum dot (QD) under varying magnetic field strengths and temperatures. Their results revealed intriguing trends, with entropy exhibiting monotonic growth at lower temperatures, largely independent of magnetic field strength, but highly influenced by the magnetic field at elevated temperatures. Furthermore, their work highlighted peaks in heat capacity and magnetic susceptibility at low temperatures. Kria et al. [27] embarked on a theoretical exploration of an AlAs/GaAs cylindrical core-shell quantum dot, evaluating both linear and nonlinear absorption coefficients and refractive indices related to the $1s-1p$ transition of a donor impurity. Their numerical simulations revealed the sensitivity of optical responses to various parameters, including shell thickness, impurity position, temperature, and pressure. Notably, their findings indicated significant blue shifts in absorption spectra for thinner shells.

In the present study, we dive into the influence of a homogeneous magnetic field, applied parallel to the axis of a hollow cylindrical quantum wire (HC), on the optical properties of the quantum wire. Our focus encompasses absorption coefficients and refractive index changes, examined up to the third order. To achieve this, we utilize wave functions obtained as solutions of the Schrödinger equation within the effective mass approximation. Additionally, we explore the impact of the inner radius of the HC on optical properties. This paper unfolds as follows: Section 2 provides a detailed exposition of the theoretical framework, while Section 3 elucidates the results and initiates discussions. Conclusive remarks are laid in Section 4.

2 Theoretical framework

The system under study is a hollow cylindrical quantum wire of inner and outer radii R_1 and R_2. The electric confining of this system is solely due to the infinite potential barriers at the surfaces and is taken as infinity elsewhere. The hollow cylinder (HC) is in the presence of a homogeneous external magnetic field applied parallel to the axis of the wire. The vector potential associated with the magnetic field is taken in the gauge $(0,\ B\rho/2,\ 0)$. Owing to the symmetry of the problem, the wave function is sought in the form $\Psi(\rho,\ \phi,\ z) = C_{ml}\chi(\rho)\exp(im\phi)\exp(ik_z z)$, where C_{ml} is normalization constant, m is the azimuthal quantum number, k_z is the axial wave vector, and $\chi(\rho)$ is the radial part of the total wave function and is found to satisfy the differential equation

$$\frac{1}{\rho}\frac{d}{d\rho}\left(\rho\frac{d}{d\rho}\chi(\rho)\right)+\left\{\frac{2\mu}{\hbar^2}\left[E_{ml}-\frac{1}{2}m\hbar\omega_c\right]-\frac{m^2}{\rho^2}-\frac{\mu^2\omega_c^2}{4\hbar^2}\rho^2\right\}\times\chi(\rho)=0, \tag{1}$$

where μ is the effective mass of an electron, $\hbar$ is the reduced Planck's constant, and $\omega_c = eB/\mu$ is the cyclotron frequency. Solution to the above equation is a linear combination of the hypergeometric function M and the Kummer U function;

$$\chi(\rho) = C_{1ml} e^{-\varsigma/2} (\varsigma)^{|m|/2} M(a, b, \varsigma) + C_{2ml} e^{-\varsigma/2} (\varsigma)^{|m|/2} U(a, b, \varsigma) \tag{2}$$

where C_{1ml} and C_{2ml} are constants and

$$a = \frac{1 + |m|}{2} - \frac{E_{ml} - \frac{1}{2} m\hbar\omega_c}{\hbar\omega_c},$$
$$b = 1 + |m|$$

and

$$\varsigma = \frac{\mu\omega_c}{2\hbar}\rho^2.$$

Imposing the condition that the electron wave function should vanish at the walls of the HC (at $\rho = R_1$ and at $\rho = R_2$) yields the transcendental equation for the determination of the energy eigenvalues as

$$E_{ml} = \left(\frac{1 + |m|}{2} - a_0\right)\hbar\omega_c + \frac{1}{2} m\hbar\omega_c \tag{3}$$

where a_0 satisfies the condition

$$M(a_0, b, \varsigma_2) U(a_0, b, \varsigma_1) - M(a_0, b, \varsigma_1) U(a_0, b, \varsigma_2) = 0 \tag{4}$$

with $\varsigma_i = \frac{\mu\omega_c}{2\hbar} R_i^2$, where $i = 1, 2$ for ς evaluated at the inner and outer radii, respectively.

2.1 Absorption coefficients and refractive index changes

We consider circularly polarized light $\vec{E}(t) = (E_0\hat{\lambda}e^{i\omega t} + E_0\hat{\lambda}e^{-i\omega t})\hat{k}$, propagating parallel to the axis of the cylindrical quantum structure. Here, E_0 is the magnitude of the electric field component of the EM radiation field of polarization vector $\hat{\lambda}$ and angular frequency ω. Under the influence of a perturbing field, the evolution of an electron state density matrix $\hat{D}$ can be studied by utilizing the time-dependent Liouville equation [28]

$$\frac{\partial \hat{D}_{ij}}{\partial t} = \frac{1}{i\hbar}\left[\hat{H}_0 - \hat{M}\vec{E}(t), \hat{D}_{ij}\right]_{ij} - \Gamma_{ij}\left(\hat{D} - \hat{D}^{(0)}\right)_{ij}. \tag{5}$$

$\hat{H}_0$ is the Hamiltonian of the unperturbed system, $\hat{M}\vec{E}(t) = -e\hat{r}\vec{E}(t)$ is the perturbing term in which e is charge of an electron, and $\hat{r}$ the radial position vector. Γ_{ij} is the rate at which $\hat{D}$ relaxes to $\hat{D}^{(0)}$ and [] is the commutator. Iterative methods can be used to solve the above equation (Eq. 5), that is,

$$\hat{D}(t) = \sum_n \hat{D}^{(n)}(t) \tag{6}$$

with

$$\frac{\partial \hat{D}_{ij}^{(n+1)}}{\partial t} = \frac{1}{i\hbar}\left\{\left[\hat{H}_0, \hat{D}_{ij}^{(n+1)}\right]_{ij} - i\hbar\Gamma_{ij}\hat{D}_{ij}^{(n+1)}\right\} - \frac{1}{i\hbar}\left[e\hat{r}, \hat{D}_{ij}^{(n)}\right]E(t). \tag{7}$$

When an electromagnetic radiation is incident upon a material, the electric field of the radiation slightly displaces the nuclei and electrons in opposite directions, resulting in a slight polarization of the medium. This polarization can be expressed in a form similar to that in Eq. (6) as (here considered up to third order),

$$P(t) = \epsilon_0\left[\chi_{sus}(\hbar\omega, I_\omega) E_0 e^{-i\omega t} + \chi_{sus}(-\hbar\omega, I_\omega) E_0 e^{i\omega t}\right]. \tag{8}$$

where ϵ_0 is the absolute dielectric permittivity of the classical vacuum and χ_{sus} is the Fourier transform of linear susceptibility. The electronic polarization of n^{th} order can be calculated according to [28]

$$P^{(n)}(t) = \frac{1}{V} Tr\left(erD^{(n)}\right) \tag{9}$$

where V is the volume of the HC and Tr refers to the trace, that is, summation of all the diagonal elements of the matrix. Absorption coefficient can be obtained from susceptibility as

$$\alpha(\hbar\omega, I_\omega) = \omega\sqrt{\frac{\mu_0}{\epsilon_r}} Im[\epsilon_0\ \chi_{\text{sus}}(\hbar\omega, I_\omega)] \tag{10}$$

while change in refractive index is

$$\frac{\Delta n}{(n_r)} = \text{Re}\left[\frac{\chi_{\text{sus}}(\hbar\omega, I_\omega)}{2n_r}\right]. \tag{11}$$

The intensity of an electromagnetic radiation in some medium is attenuated according to $I = I_\omega \exp(-\alpha x)$, where I_ω is the intensity of the incident EM radiation, x the distance penetrated by the EM radiation inside the medium and α the absorption coefficient of the medium. The absorption coefficient (AC) of a crystal evaluated up to third order is expressed as [29, 30]

$$\alpha(\hbar\omega, I_\omega) = \alpha^{(1)}(\hbar\omega) + \alpha^{(3)}(\hbar\omega, I_\omega). \tag{12}$$

where

$$\alpha^{(1)}(\hbar\omega) = \frac{4\pi\alpha_{FS}\sigma_V}{n_r e^2}\hbar\omega|M_{fi}|^2\delta\big(\Delta E_{fi} - \hbar\omega\big), \tag{13}$$

and

$$\alpha^{(3)}(\hbar\omega, I_\omega) = \frac{32\pi^2\alpha_{FS}^2\sigma_V I_\omega}{n_r^2 e^4 \hbar\Gamma_{ff}}\hbar\omega|M_{fi}|^4\delta\big(\Delta E_{fi} - \hbar\omega\big)^2(1 - \varpi_\alpha), \tag{14}$$

with

$$\varpi_\alpha = \frac{|M_{ff} - M_{ii}|^2}{4|M_{fi}|^2} \times \frac{\big(\hbar\omega - \Delta E_{fi}\big)^2 - \big(\hbar\Gamma_{fi}\big)^2 + 2\Delta E_{fi}\big(\Delta E_{fi} - \hbar\omega\big)}{\big(\Delta E_{fi}\big)^2 + \big(\hbar\Gamma_{fi}\big)^2}. \tag{15}$$

Here, σ_V is the electron volume density, α_{FS} is the fine structure constant, and n_r is the refractive index of the crystal. M_{fi} are the matrix elements coupling one state $|i\rangle$ to the other $|f\rangle$, while $\hbar\Gamma_{fi}$ are the line widths associated with the different states indicated by the subscripts.

The corresponding first- and third-order contributions to the refractive index change are given by [29]

$$\frac{\Delta n^{(1)}}{(n_r)} = \frac{e^2\sigma_V}{2\,\epsilon_r}|M_{fi}|^2\frac{\Delta E_{fi} - \hbar\omega}{\big(\Delta E_{fi}\big)^2 - \big(\hbar\Gamma_{ff}\big)^2}, \tag{16}$$

and

$$\frac{\Delta n^{(3)}}{n_r} = \frac{\mu_0 c I_\omega}{4\,\epsilon_r\, n_r^2}\frac{e^4\sigma_V|M_{fi}|^2}{\Big[\big(\Delta E_{fi}\big)^2 - \big(\hbar\Gamma_{fi}\big)^2\Big]^2}\varpi_n, \tag{17}$$

where

$$\varpi_n = 4|M_{fi}|^2\big(\Delta E_{fi} - \hbar\omega\big) - |M_{ff} - M_{ii}|^2\frac{\Delta E_{fi}\big(\Delta E_{fi} - \hbar\omega\big)^2 - \big(\hbar\Gamma_{fi}\big)^2\big(3\Delta E_{fi} - 2\hbar\omega\big)}{\big(\Delta E_{fi}\big)^2 + \big(\hbar\Gamma_{fi}\big)^2} \tag{18}$$

and ϵ_r is the permeability of the material. In Eqs. (16) and (17), the energy conserving delta function has been replaced by the Lorentzian function. However, the terms in Eqs. (16) and (17) emerge naturally in the electron density matrix formulation. For computational purpose, the delta function in Eqs. (13) and (14) also has been replaced the Lorentzian function. The total change in refractive index (considered to third order) is

$$\frac{\Delta n}{n_r} = \frac{\Delta n^{(1)}}{n_r} + \frac{\Delta n^{(3)}}{n_r}. \tag{19}$$

3 Results

The key parameters used in these computations, relevant to the system of GaAs, are $\mu = 0.067\mathrm{m_e}$, $\mathrm{m_e}$ being mass of the free electron, $\sigma_V = 3 \times 10^{22}\mathrm{m}^{-3}$ and $\hbar\Gamma_{ij} = 3.3$ meV [31]. Figure 1 depicts transition energies, $\Delta E_{fi} = |E_f - E_i|$, as functions of the magnetic field energy in a hollow cylinders (HCs) of inner radii $R_1 = 50$ Å (marked 50) and $R_1 = 100$ Å, (marked 100) compared with those for a solid cylinder ($R_1 = 0$ (SC)). The outer radius of both the HCs and the SC is $R_2 = 300$ Å. The solid plots correspond to transition energies between the $m = 0$ state and the $m = 1$ state, the latter being the final state when absorption is in question. The dashed are transition energies between the $m = 0$ state and the $m = -1$ state, the former ($m = 0$ state) being the initial state for magnetic field energies less than the inflection points marked by the open circles, while for magnetic field energies beyond the inflection points, the $m = -1$ state is the initial state, when absorption is considered. The horizontal lines are the values equal to the energies of EM radiation used in Figs. 3a, b, and 6. As can be seen from the figure, whereas the $m = 0 \rightarrow m = 1$ transition energies merely increase with increasing magnetic field energy, those between the $m = 0$ and the $m = -1$ states decrease with increasing magnetic field energy when the $m = -1$ state is the final state, and increase when the $m = 0$ is the final state. This is because of the Zeeman splitting [32, 33]

Figure 2 shows the variation of the AC with the energy of the EM field for the $m = 0 \rightarrow m = \pm 1$ transitions in the absence ($\beta_1 = \hbar\omega_c = 0$) and presence of the magnetic field ($\beta_2 = \hbar\omega_c = 5$ meV). The solid plots marked β_2 are for the $m = 0 \rightarrow m = 1$

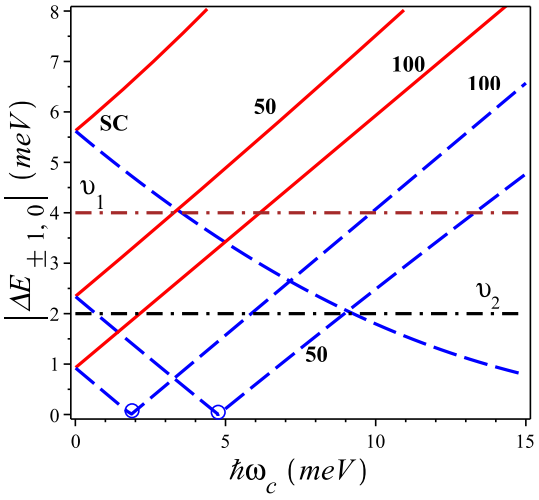

Fig. 1 Transition energies as functions of the magnetic field energy for an SC ($R_1 = 0$) and for HCs of inner radii $R_1 = 50$ Å and $R_1 = 100$ Å, all of outer radii $R_2 = 300$ Å. The solid plots are for the $m = 0 \rightarrow m = 1$ transition, while the dashed plots are for the $m = 0 \rightarrow m = -1$ transition. The horizontal dashed lines (labeled υ_1 and υ_2) represent the values of the EM radiation used in Figs. 3a, b, and 6

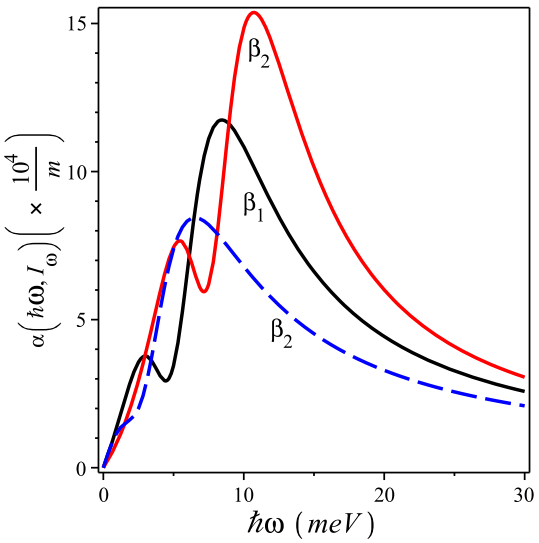

Fig. 2 Dependence of the absorption coefficient on energy of the EM radiation of intensity $I_\omega = 200\ MW/m^2$ for an HC of inner and outer radii of $R_1 = 50$ Å and $R_2 = 300$ Å. The plot marked β_1 corresponds to the absence of the magnetic field ($\hbar\omega_c = 0$), while those marked β_2 correspond to a magnetic field energy $\hbar\omega_c = 5\ meV$. Of the plots marked β_2, the solid are for the $m = 0 \rightarrow m = 1$ transition, while the dashed are for the $m = 0 \rightarrow m = -1$ transition

transition, while the dashed plots marked β_2 are for the $m = 0 \rightarrow m = -1$ transition. Here, the intensity of the EM radiation is $I_\omega = 200$ MW/m^2. In the absence of the magnetic field, the $m = \pm 1$ states are degenerate, hence absorption coefficients for transitions from the ground state to these states are identical. The magnetic field lifts the degeneracies of the $m \neq 0$ states of opposite signs. Consequently, ACs for $m = 0 \rightarrow m = 1$ transition are distinct from those of $m = 0 \rightarrow m = -1$ transition. The other effect of the magnetic field is in enhancing the magnitude of the AC for $m = 0 \rightarrow m = 1$ transition while dwindling that of the $m = 0 \rightarrow m = -1$ transition.

Figure 3 shows variations of the AC of a cylindrical quantum wire with the magnetic field energy for different values of intensity of the incident EM radiation (a) and for different values of the inner radius (b). The solid curves are for the $m = 0 \rightarrow m = 1$ transition, while the dashed plots are for the $m = 0 \rightarrow m = -1$ transition. In Fig 3a, $I_{01} = I_\omega = 0$ and $I_{02} = I_\omega = 75$ MW/m^2. As can be viewed in Fig. 1, the radiation of energy chosen here is less than the zero magnetic field transition energies for an HC of these dimensions ($\Delta E_{ml}(\hbar\omega_c = 0)$). Consequently, absorption will only occur for the $m = 0 \rightarrow m = -1$ transition and not for the $m = 0 \rightarrow m = 1$ transition as the magnetic field energy is increased. Thus, as Fig. 1 also suggests, the variation of the AC with the magnetic field energy is characterized by two peaks involving transition between the $m = 0$ and $m = -1$ states, the first corresponding to the $m = 0 \rightarrow m = -1$ transition and the other to the $m = -1 \rightarrow m = 0$ transition. Increase in intensity of the radiation reduces the AC considered to third order. Figure 3b compares the effect of I_ω (= 100 MW/m^2) on the AC for an SC and an HC as a function of the magnetic field energy. The energy of the incident EM radiation ($\hbar\omega$) is slightly lower than zero magnetic field ($\hbar\omega_c = 0$) $m = 0 \rightarrow m = \pm 1$ transition energies for a solid nanocylinder (SC) but not for the HC. This implies that for EM radiation of this energy, absorption due to the $m = 0 \rightarrow m = 1$ transition will not be possible in this SC but would in an HC of the same outer radius. Absorption due to the $m = 0 \rightarrow m = -1$ transition will occur in an SC when $m = -1$ state is the final state and occur in an HC when the $m = 0$ state is the final state.

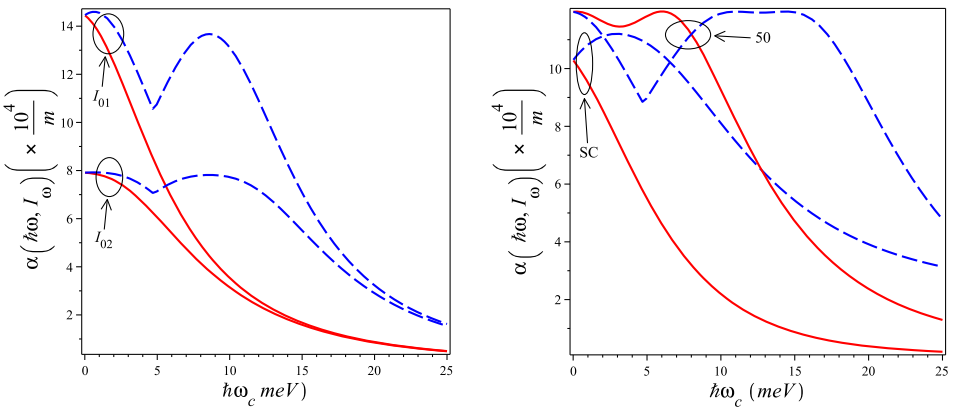

(a) AC for an HC of inner and outer radii $R_1 = 50$ Å and $R_2 = 300$ Å. The plots with greater intercept correspond to $I_\omega = 0$ while those with smaller intercept are for $I_\omega = 75\ MW/m^2$. The energy of the incident EM radiation of intensity has been taken as $\hbar\omega = 2\ meV$.

(b) AC for an SC ($R_1 = 0$) of radius $R_2 = R = 300$ Å and for HC of inner and outer radii $R_1 = 50$ Å and $R_2 = 300$ Å. Here, the energy of the incident EM radiation of intensity $I_\omega = 100\ MW/m^2$ has been taken as $\hbar\omega = 4\ meV$.

Fig. 3 AC as a function of the magnetic field energy for an HC, for different values of intensity of the EM radiation (a) and for different values of the inner radius (b). The solid plots are associated with the $m = 0 \rightarrow m = 1$ transition, while the dashed plots correspond to the $m = 0 \rightarrow m = -1$ transition

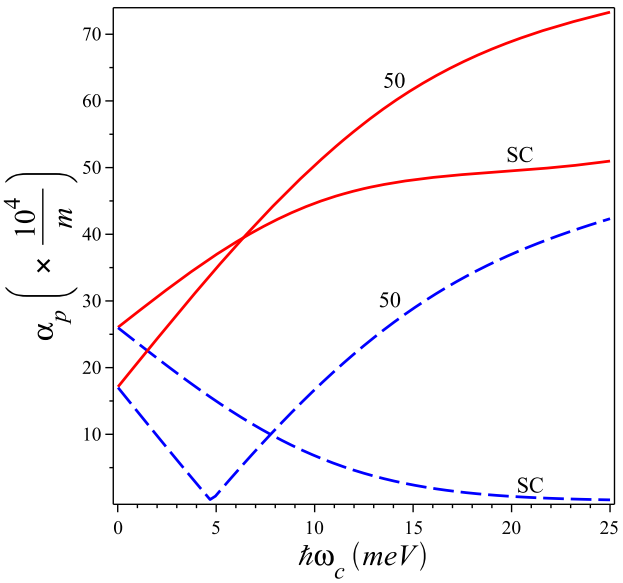

Fig. 4 Peaks of the linear AC as functions of the magnetic field energy for an SC ($R_1 = 0$) of radius $R_2 = R = 300$ Å, and for an HC of inner and outer radii $R_1 = 50$ Å and $R_2 = 300$ Å. The solid curves are associated with the $m = 0 \rightarrow m = 1$ transition, while the dashed plots correspond to the $m = 0 \rightarrow m = -1$ transition

Figure 4 shows the dependence of peaks of the linear AC ($I_\omega = 0$) on the magnetic field energy for a SC ($R = 300$ Å) and for a HC of radii $R_1 = 50$ Å and $R_2 = 300$ Å (marked 50)., for $I_\omega = 0$. The solid plots are associated with the $m = 0 \rightarrow m = 1$ transition, while the dashed plots correspond to the $m = 0 \rightarrow m = -1$ transition. It is seen from Fig. 4 that for zero magnetic field, the presence of a hole leads to a reduction of the peaks of AC. However, the inner radius increases the degree at which peaks of the AC increase with the magnetic field energy. This means that in the presence of magnetic fields, HCs can outperform SCs in absorbing radiation of specific energy.

Figure 5 shows the dependence of the change in refractive index (CRI) on energy of the incident EM radiation field for an HC of inner and outer radii $R_1 = 50$ Å and $R_2 = 300$ Å, for different values on intensity of the EM wave (a) and for different values of the magnetic field energy (b). The different curves in (a) have been generated for different values of the intensity of the incident EM radiation field, in increments of 100 MW/m^2 from $I_\omega = 0$ up to $I_\omega = 400$ MW/m^2, going down the vertical axis. The linear CRI ($I_\omega = 0$) as a function of energy of the EM radiation is characterized by regions where it increases with increasing energy (normal dispersion region) and regions where it decreases with increasing energy of EM radiation (anomalous dispersion region). As the intensity of incident increases, CRI develops normal dispersion in the anomalous region. Additionally, the presence of the inner radius enhances absorption associated with negative m values. This implies that presence of magnetic field, the combined absorption comprising of contributions from transitions involving states of opposite m values will be greatly enhanced, particularly for high values of the magnetic field. In Fig. 5b, the fractional change in refractive index of an HC has been plotted as a function of energy of the EM radiation of intensity $I_\omega = 200$ MW/m^2 for different values of the magnetic field energy. The line labeled β_1 corresponds to $m = 0 \rightarrow m = \pm 1$ transitions in the absence of the magnetic field. The solid line marked β_2 correspond to the

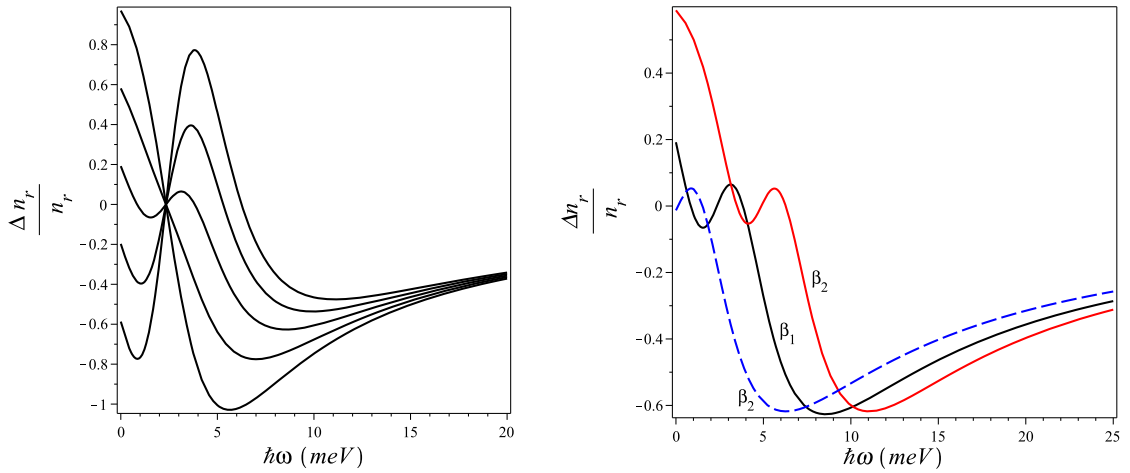

(a) CRI for different values of intensity of the incident EM radiation, and in order of decreasing vertical axis intercepts: $I_\omega = 0$, $I_\omega = 100\ MW/m^2$, $I_\omega = 200\ MW/m^2$, $I_\omega = 300\ MW/m^2$ and $I_\omega = 400\ MW/m^2$. The other relevant parameters are $R_1 = 50\ \mathring{A}$, $R_2 = 300\ \mathring{A}$ and $\hbar\omega_c = 0$.

(b) CRI for different values magnetic field energy: β_1 corresponds to the absence of the magnetic field ($\hbar\omega_c = 0$) while β_2 correspond a magnetic field of energy $\hbar\omega_c = 5\ meV$. Here, intensity of the EM radiation is $I_\omega = 200\ MW/m^2$.

Fig. 5 Dependence of CRI of an HC of inner and outer radii $R_1 = 50$ Å and $R_2 = 300$ Å on energy of the EM radiation for different values of intensity of the incident EM radiation (a) and for different values of the magnetic field energy (b)

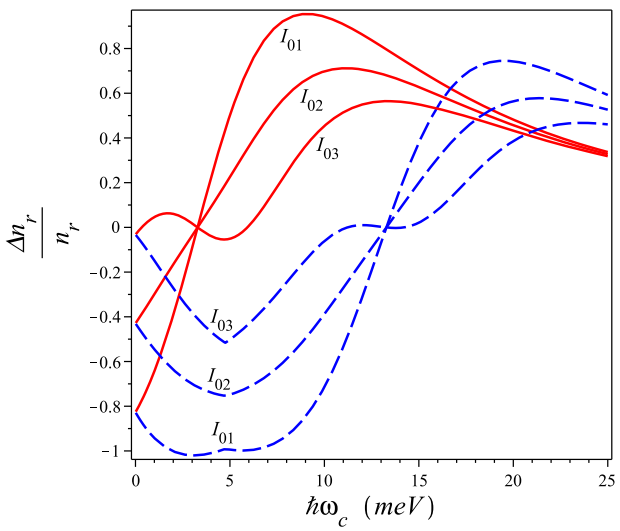

Fig. 6 CRI as a function of the magnetic field energy for an HC of inner and outer radii $R_1 = 50$ Å and $R_2 = 300$ Å, for $\hbar\omega = 4\ meV$. The different pairs have been plotted for different intensities: $I_{01} = I_\omega = 0$, $I_{02} = I_\omega = 100$ MW/m^2 and $I_{03} = I_\omega = 200$ MW/m^2. The solid curves are associated with the $m = 0 \rightarrow m = 1$ transition, while the dashed plots correspond to the $m = 0 \rightarrow m = -1$ transition

$m = 0 \rightarrow m = 1$ transition, while the dashed curve is associated with the $m = 0 \rightarrow = -1$ transition, both in a magnetic field of energy $\hbar\omega_c = 5\ meV$. The magnetic field blueshifts the CRI for the $m = 0 \rightarrow m = 1$ transition. For the $m = 0 \rightarrow = -1$ transition, increase in the magnetic field initially redshifts the CRI up to the magnetic field corresponding to the inflection points indicated in Fig. 1, beyond which increase in the field blueshifts CRI.

Figure 6 shows variations of CRI of a HC of radii $R_1 = 50$ Å and $R_2 = 300$ Å with the magnetic field energy for some values of the intensity of electromagnetic radiation: $I_\omega = 0$, 100 and 200 MW/m^2. In the figure, the solid curves are associated with the $m = 0 \rightarrow = 1$ transition, while the dashed plots correspond to the $m = 0 \rightarrow = -1$ transition. With reference to Fig. 1, the $R_1 = 50$ Å graph for the $m = 0 \rightarrow m = \pm 1$ transition energies intersects the $E = \hbar\omega = 4$ meV at $\hbar\omega_c \approx 3.2$ meV (for the $m = 0 \rightarrow m = 1$ transition) and at $\hbar\omega_c \approx 13.5$ meV (for the $m = 0 \rightarrow m = -1$ transition). Consequently, the CRI vanish at these points, regardless of intensity of the applied EM field. The figure suggests that application of magnetic field can be used to modify the optical properties of quantum structures, by modulating the refractive index. Additionally, the magnetic field modifies the refractive index differently depending on whether transitions involve the positive or negative m states. This imbues the nanostructure with different refractive indices that correspond to the signs of the m values of the states between which transitions occur, which will not occur in the absence of the externally applied magnetic field.

4 Conclusion

Optical properties of a *GaAs* hollow cylindrical quantum wire in the presence of a magnetic field have been studied. The homogeneous magnetic field was considered to be applied parallel to the axis of the cylindrical quantum wire. The optical properties investigated are optical absorption coefficient (AC) and change in refractive index (CRI), both evaluated up to third order. The research was mainly concerned with the effects of intensity of the electromagnetic radiation, inner radius and strength of the externally applied magnetic field. Increase in intensity of incident electromagnetic radiation decreased the magnitude of the AC. The intensity also introduced a normal dispersion in the anomalous region of the variation of the CRI as a function of energy of the incident electromagnetic radiation. The magnetic field split the absorption coefficient into two branches that corresponding to transitions involving the states with angular momentum in one direction, and another corresponding to transitions involving angular momentum in the opposite direction. This is due to the Zeeman splitting. One other effect that magnetic field had on the CRI was blueshifting the CRI concerning the $m = 0 \rightarrow m = 1$ transition and redshifting the CRI for the $m = 0 \rightarrow m = -1$ transition. Results also indicate that the presence of the inner radius enhanced absorption coefficient in two ways: by increasing the magnitude of the AC, and second, by facilitating an additional transition ($m = -1 \rightarrow m = 0$) that does not occur in a solid cylindrical nanostructure. Further work to improve this research may be to evaluate the effect of tilt of the applied magnetic field relative of axis of the nanowire on the optical properties.

Acknowledgements LMP acknowledges financial support from the ANID through Convocatoria Nacional Subvención a Instalación en la Academia Convocatoria Año 2021, Grant SA77210040 and from FONDECYT 1240985

Funding Open access funding provided by University of Botswana.

Data Availability Statement This manuscript has no associated data.

Open Access This article is licensed under a Creative Commons Attribution 4.0 International License, which permits use, sharing, adaptation, distribution and reproduction in any medium or format, as long as you give appropriate credit to the original author(s) and the source, provide a link to the Creative Commons licence, and indicate if changes were made. The images or other third party material in this article are included in the article's Creative Commons licence, unless indicated otherwise in a credit line to the material. If material is not included in the article's Creative Commons licence and your intended use is not permitted by statutory regulation or exceeds the permitted use, you will need to obtain permission directly from the copyright holder. To view a copy of this licence, visit http://creativecommons.org/licenses/by/4.0/.

References

1. J. Drbohlavova, V. Adam, R. Kizek, J. Hubalek, Quantum dots characterization, preparation and usage in biological systems. Int. J. Mol. Sci. **10**, 656–673 (2009)
2. P. Kluson, M. Drobek, H. Bartkova, I. Budil, Welcome in the nanoworld. Chem. Listy **101**, 262–272 (2007)
3. R.S. Wagner, W.C. Ellis, Vapor-liquid-solid mechanism of single crystal growth. Appl. Phys. Lett. **4**(5), 89–90 (1964)
4. Z.Y. Zeng, Y. Xiang, L.D. Zhang, Eur. Phys. J. B **17**, 699 (2000)
5. J.-F. You, Q. Zhao, Z.-H. Zhang, J.-H. Yuan, K.-X. Guo, E. Feddi, The effect of temperature, hydrostatic pressure and magnetic field on the nonlinear optical properties of algaas/gaas semi-parabolic quantum well. Int. J. Mod. Phys. B **33**(27), 1950325 (2019)
6. F. Nammas, Thermodynamic properties of two electrons quantum dot with harmonic interaction. Phys. A **508**, 187–198 (2018)
7. F. Nammas, H.G.M.A.-S.A. Sandouqa, Thermodynamic properties of two-dimensional few-electrons quantum dot using the static fluctuation approximation (sfa). Phys. B **406**(24), 4671–4677 (2011)
8. K.L. Jahan, B. Boyacioglu, A. Chatterjee, Effect of confinement potential shape on the electronic, thermodynamic, magnetic and transport properties of a gaas quantum dot at finite temperature. Sci. Rep. **9**(1), 1–10 (2019)
9. N.T. Nguyen, F. Peeters, Magnetic field dependence of the many-electron states in a magnetic quantum dot: the ferromagnetic-antiferromagnetic transition. Phys. Rev. B **78**(4), 045321 (2008)
10. B. Boyacioglu, A. Chatterjee, Heat capacity and entropy of a gaas quantum dot with gaussian confinement. J. Appl. Phys. **112**(8), 083514 (2012)
11. S. Gumber, M. Kumar, M. Gambhir, M. Mohan, P.K. Jha, Thermal and magnetic properties of cylindrical quantum dot with asymmetric confinement. Can. J. Phys. **93**(11), 1264–1268 (2015)
12. S. Gumber, M. Kumar, P.K. Jha, M. Mohan, Thermodynamic behavior of rashba quantum dot in the presence of magnetic field. Chin. Phys. B **25**(5), 056502 (2016)
13. Y. Sun, P.-F. Li, Z.-W. Wang, Resolution of polaron spin states by the infrared absorption in monolayer transition metal dichalcogenides. Phys. E **124**, 114302 (2020)
14. Y. Sun, Z.-Q. Li, W.-Z. Wang, Infrared optical absorption of magnetopolaron resonance states in graphene on thepolar substrates. J. Phys. Condens. Matter **32**(42), 425005 (2020). https://doi.org/10.1088/1361-648X/aba293
15. X. Zhang, C.W. Pinion, J.D. Christesen, C.J. Flynn, T.A. Celano, J.F. Cahoon, Horizontal silicon nanowires with radial p-n junctions: a platform for unconventional solar cells. J. Phys. Chem. Lett. **4**(12), 2002–2009 (2013)
16. J.J. Wierer Jr., Q. Li, D.D. Koleske, S.R. Lee, G.T. Wang, Iii-nitride core-shell nanowire arrayed solar cells. Nanotechnology **23**(19), 194007 (2012)
17. Z. Gui, G. Xiong, F. Gao, Microelectron. J. **38**, 447 (2007)
18. T. Akiyama, O. Wada, H. Kuwatsuka, T. Simoyama, Y. Nakata, K. Mukai, M. Sugawara, H. Isikawa, Appl. Phys. Lett. **77**, 1753 (2000)
19. M. Balkanski, R.F. Wallis, Semiconductor physics and applications. Oxford Univ. Press (2000). https://doi.org/10.5772/63493
20. N. Aghoutane, M. El-Yadri, A. El Aouami, E. Feddi, G. Long, M. Sadoqi, F. Dujardin, C.V. Nguyen, N.N. Hieu, H.V. Phuc, Excitonic nonlinear optical properties in aln/gan spherical core/shell quantum dots under pressure. MRS Commun. **222**, 1–7 (2019)
21. A. Talbi, E. Feddi, A. Oukerroum, E. Assaid, F. Dujardin, M. Addou, Theoretical investigation of single dopant in core/shell nanocrystal in magnetic field. Superlattices Microstruct. **85**, 581–591 (2015)

22. A. Talbi, E. Feddi, A. Zouitine, M. El Haouari, M. Zazoui, A. Oukerroum, F. Dujardin, E. Assaid, M. Addou, Control of the binding energy by tuning the single dopant position, magnetic field strength and shell thickness in zns/cdse core/shell quantum dot. Phys. E **84**, 303–309 (2016)
23. E. Feddi, M. El-Yadri, F. Dujardin, R. Restrepo, C. Duque, Photoionization cross section and binding energy of single dopant in hollow cylindrical core/shell quantum dot. J. Appl. Phys. **121**(6), 064303 (2017)
24. K.-H. Kim, Y.-S. No, Subwavelength core/shell cylindrical nanostructures for novel plasmonic and metamaterial devices. Nano Converg. **4**, 32 (2017)
25. M.G. Barseghyan, M.E. Mora-Ramos, C.A. Duque, Hydrostatic pressure, impurity position and electric and magnetic field effects on the binding energy and photo-ionization cross section of a hydrogenic donor impurity in an inas pöschl-teller quantum ring. Eur. Phys. J. B **84**, 265–271 (2011)
26. R. Khordad, H. Sedehi, Thermodynamic properties of a double ring-shaped quantum dot at low and high temperatures. J. Low Temp. Phys. **190**(3–4), 200–212 (2018)
27. M. Kria, M. El Yadri, N. Aghoutane, L.M. Pérez, D. Laroze, E. Feddi, Forecasting and analysis of nonlinear optical responses by tuning the thickness of a doped hollow cylindrical quantum dot. Chinese J. Phys. **66**, 444–452 (2020)
28. R. Khordad, Third harmonic generation in a double ring-shaped quantum dot under electron phonon interaction. Opt. Commun. **391**, 121–127 (2017). https://doi.org/10.1016/j.optcom.2017.01.017
29. N. Arunachalam, A.J. Peter, C.K. Yoo, Exciton optical absorption coefficients and refractive index changes in a strained inas/gaas quantum wire: the effect of the magnetic field. J. Lumi. **132**, 1311–1317 (2012)
30. W.-F. Xie, Linear and nonlinear optical absorptions of a donor impurity in spherical quantum dots. Commun. Theor. Phys. **52**(1), 155–158 (2009). https://doi.org/10.1088/0253-6102/52/1/33
31. F. Aydin, H. Sari, E. Kasapoglu, S. Sakiroglu, I. Sökmen, The anisotropy effects on the shallow-donor impurity states and optical transitions in quantum dots. Eur. Phys. J. Plus **136**, 832 (2021)
32. N.C. Constantinou, M. Masale, D.R. Tilley, The zeeman splitting of quasi-one dimensional electron subbands. J. Phys.: Condens. Matter **4**, 4499–4508 (1992)
33. M. Masale, Oscillator strengths for optical transitions in a hollow cylinder. Phys. B: Condens. Matter **292**(3–4), 241–249 (2000)